High-entropy argyrodite glass–ceramic electrolytes for all-solid-state batteries

OPEN ACCESS
IOP Publishing | Songshan Lake Materials Laboratory

MATERIALS FUTURES

Mater. Futures 4 (2025) 025105 (12pp) https://doi.org/10.1088/2752-5724/adde76

High-entropy argyrodite glass–ceramic electrolytes for all-solid-state batteries

Jing Lin[1], Mareen Schaller[2], Ruizhuo Zhang[1], Volodymyr Baran[3], Hao Liu[2], Ziming Ding[4], Sylvio Indris[2,5], Aleksandr Kondrakov[1,6], Torsten Brezesinski[1,*] and Florian Strauss[1,*]

[1] Battery and Electrochemistry Laboratory (BELLA), Institute of Nanotechnology, Karlsruhe Institute of Technology (KIT), Kaiserstr. 12, 76131 Karlsruhe, Germany
[2] Institute for Applied Materials–Energy Storage Systems, Karlsruhe Institute of Technology (KIT), Kaiserstr. 12, 76131 Karlsruhe, Germany
[3] Deutsches Elektronen-Synchrotron DESY, Notkestr. 85, 22607 Hamburg, Germany
[4] Institute of Nanotechnology, Karlsruhe Institute of Technology (KIT), Kaiserstr. 12, 76131 Karlsruhe, Germany
[5] Applied Chemistry and Engineering Research Centre of Excellence (ACER CoE), Université Mohammed VI Polytechnique (UM6P), Lot 660, Hay Moulay Rachid, Ben Guerir 43150, Morocco
[6] BASF SE, Carl-Bosch-Str. 38, 67056 Ludwigshafen, Germany

E-mail: torsten.brezesinski@kit.edu and florian.strauss@kit.edu

Received 7 March 2025, revised 2 May 2025
Accepted for publication 27 May 2025
Published 20 June 2025

Abstract

Lithium argyrodite superionic conductors with the general formula Li_6PS_5X (X = Cl, Br, I) have been intensively investigated in recent years and successfully adopted in the field of solid-state batteries (SSBs). The transport properties of argyrodite solid electrolytes (SEs) usually strongly depend on the degree of occupational disorder. Increasing disorder through complex doping or substitution has been shown to directly affect ionic conductivity. Herein, we explore a high-entropy lithium argyrodite of nominal composition $Li_{6.6}[P_{0.2}Si_{0.2}Sn_{0.2}Ge_{0.2}Sb_{0.2}]S_5I$. This material can be readily prepared by mechanochemistry. Using complementary diffraction techniques, nuclear magnetic resonance spectroscopy, and charge-transport measurements, we show that upon tailoring crystallinity and defect concentration by post-annealing at temperatures up to 220 °C, a high room-temperature ionic conductivity of about 0.9 mS cm^{-1} (~4.4 mS cm^{-1} bulk conductivity) can be achieved. Both the as-prepared and annealed (at 220 °C) samples were tested in pellet-stack SSB cells. The mechanochemically prepared glass–ceramic SE was found to exhibit superior performance, even outperforming commercially available Li_6PS_5Cl. Collectively, the results highlight the importance of considering structural aspects across different length scales when optimizing the properties of lithium argyrodites for SSB applications.

* Authors to whom any correspondence should be addressed.

Supplementary material for this article is available online

Keywords: high-entropy materials, solid electrolytes, solid-state batteries

1. Introduction

With the ever-increasing demand for electrochemical energy storage solutions, solid-state batteries (SSBs) have emerged as a promising technology due to their high energy and powder densities and intrinsic safety [1–3]. Solid electrolytes (SEs) are key materials enabling high-performance SSBs. Thus, the ongoing pursuit of exploring advanced lithium-ion conductors should focus on combining high room-temperature ionic conductivity with robust (electro)chemical stability and facile processability [4, 5]. In recent years, lithium thiophosphates, including $Li_{10}GeP_2S_{12}$ (LGPS), $Li_2S{-}P_2S_5$ glass–ceramics, and Li_6PS_5X (X = Cl, Br, I) argyrodites, have garnered considerable attention owing to their softness and high ionic conductivities, which may be similar to or even exceed those of liquid electrolytes [6–10]. Crystalline lithium argyrodites, in particular Li_6PS_5X with X = Cl, Br, enable fast lithium diffusion due to the presence of strongly disordered sublattices with a high density of S^{2-}/X^- antisite defects, leading to ionic conductivities of $\sigma_{\text{ion, 25 °C}} > 1$ mS cm^{-1} [9]. In contrast, Li_6PS_5I SEs typically exhibit relatively low ionic conductivities (on the order of 10^{-3} mS cm^{-1}) because of the lack of site inversion and, therefore, unfavorable $Li^+{-}Li^+$ jump distances. However, it has been shown that both simple and complex aliovalent substitutions at the phosphorus site in Li_6PS_5I, e.g. $Li_{6+x}P_{1-x}Ge_xS_5I$ or $Li_{6.5}[P_{0.25}Si_{0.25}Ge_{0.25}Sb_{0.25}]S_5I$, can increase the ionic conductivity up to about 10 mS cm^{-1}, which is primarily due to the shortened $Li^+{-}Li^+$ jump distances resulting from increased S^{2-}/I^- site inversions [10–13]. Alternatively, nanostructuring and tailoring of the defect density via high-energy ball milling have been demonstrated to cause a several-fold increase in ionic conductivity of Li_6PS_5I [14]. Unlike the highly crystalline Li_6PS_5I, where (long-range) diffusion is hindered by long $Li^+{-}Li^+$ jump distances, nanocrystalline forms exhibit fast ion dynamics due to successful intercage jump events enabled by structural distortions. Similarly, for $1.5Li_2S{-}0.5P_2S_5{-}LiI$ glass–ceramic SEs, previous works have shown that nanostructuring, and especially amorphization, not only increases ion conductivity but also leads to favorable mechanical properties for SSB applications [15–19]. Along this line, increasing both defect density and the degree of amorphization in other poorly conducting oxide-based (crystalline) materials, such as $LiNbO_3$, Li_2TiO_3, γ-$LiAlO_2$, or $LiTaO_3$, has also been reported to enhance ionic conductivity [14, 17, 20–24]. Nonetheless, there are also examples where similar strategies have been shown to exert adverse effects on conductivity, e.g. in the case of LGPS [25]. However, whether nanostructuring is accompanied by partial amorphization or, in other words, the formation of glass–ceramic SEs (by mechanochemical synthesis starting from crystalline precursors) positively or negatively affects ionic conductivity is difficult to predict. Regardless, it has been reported that glass–ceramic SEs offer several advantages in SSBs [26]. This is linked to improved contact with the cathode active material (CAM) and better (microstructural) electrode integrity during cycling, presumably due to the softer nature of glass–ceramic compared to highly crystalline SEs. In addition, nanostructured SEs seem capable of reducing or even inhibiting dendrite formation [27–29].

Recently, multielement-substituted (compositionally complex) materials have attracted great interest, commonly referred to as high-entropy materials (HEMs) when $\Delta S_{\text{conf}} \geqslant 1.5\ R$ (with R being the universal gas constant). Here, ΔS_{conf} denotes the configurational entropy, being a statistical descriptor for occupational disorder in a given crystal structure, and can be calculated by taking into account the shared occupancy of different elements on single crystallographic sites [30]. This threshold criterion is met when at least five different elements occupy a single crystallographic site at equimolar ratios [31, 32]. The recently reported high-entropy (crystalline) SEs include garnet, perovskite, Na SuperIonic CONductor, argyrodite, and LGPS-type materials [12, 33–37]. Among them, only lithium argyrodites and LGPS-type SEs have achieved very high ionic conductivities at room temperature [38, 39]. However, to date, only four different cationic constituents have been introduced into the argyrodite structure, replacing phosphorus, conforming to the general formula $Li_{6+x}[M1_aM2_bM3_cM4_d]S_5I$, with M being P, Si, Ge, and Sb [38]. Thus, the remaining question is whether it is possible to further increase compositional complexity, i.e. configurational entropy, and how this would affect ionic conductivity, phase stability, and cycling performance.

In the present work, we explore $Li_{6.6}[P_{0.2}Si_{0.2}Sn_{0.2}Ge_{0.2}Sb_{0.2}]S_5I$-based glass–ceramics, which were prepared by mechanochemical synthesis, followed by thermal annealing. This lithium argyrodite already crystallizes to some extent during the reaction of the powder precursors used and thermally decomposes at temperatures beyond 220 °C. Subsequent annealing (after mechanochemical synthesis) increases crystallinity, which positively affects ionic conductivity, but is detrimental to the cycling performance of pellet-stack SSB cells. Overall, the results indicate that tailoring the amorphous phase fraction in glass–ceramic electrolytes may help in the development of advanced ion conductors for applications in next-generation SSBs.

2. Experimental

2.1. Synthesis

All processing steps were conducted under Ar atmosphere in a glovebox (MBraun, $[O_2]$ and $[H_2O] < 0.1$ ppm), and all precursors were used as received. Stoichiometric amounts of Li_2S

(99.99%, Sigma-Aldrich), P_2S_5 (99%, Sigma-Aldrich), GeS_2 (99.9%, Goodfellow), SiS_2 (99.99%, Goodfellow), Sb_2S_3 (99.99%, Alfa Aesar), SnS_2 (99.9%, Goodfellow), and LiI (99.999%, Sigma-Aldrich), including 10 wt.% excess sulfur (99.99%, Sigma-Aldrich) to compensate for loss during synthesis, were placed in a 70 ml zirconia milling jar. After adding 20 ZrO_2 milling balls of diameter 10 mm to the jar, the powder mixture was blended for 1 h at 250 rpm, followed by 40 h at 450 rpm. The obtained material is referred to as HEA-BM. Subsequently, about 300 mg of HEA-BM was pressed into a pellet (10 mm diameter) at 3 t, vacuum-sealed (10^{-3} mbar) in a pre-dried quartz ampule, and annealed for 72 h either at 150 °C (referred to as HEA-150) or 220 °C (referred to as HEA-220).

2.2. Inductively coupled plasma-optical emission spectroscopy (ICE-OES)

The fractions of Li, P, Si, Ge, Sb, and I were determined by ICP-OES using a Thermo Fisher Scientific ICAP 7600 DUO instrument. Powder samples were dissolved in an acid digester in a graphite furnace, and the resulting mass fraction values were obtained by performing three independent measurements.

2.3. Scanning transmission electron microscopy (STEM)

Specimen preparation was performed under Ar atmosphere in a glovebox. The dry powder was first pressed into a pellet, followed by focused ion beam milling to obtain thin lamellae for STEM investigation. Transfer to the microscope was accomplished using a Gatan cryo-transfer holder to ensure minimal air exposure. All measurements were carried out under cryogenic conditions (−175 °C) and at 300 kV using a Themis 300 (Thermo Fisher Scientific) microscope. The instrument was equipped with a DCOR probe corrector and a Super-X EDX detector. During imaging, the screen current was maintained at 60 pA.

2.4. Laboratory x-ray diffraction (XRD)

Powder samples were sealed in borosilicate capillaries from Hilgenberg (0.68 mm inner diameter, 0.01 mm wall thickness) under Ar atmosphere and subjected to XRD using an STOE Stadi-P diffractometer with a Dectris MYTHEN 1 K strip detector in Debye–Scherrer geometry. The instrument utilizes a Mo anode to generate x-rays of wavelength $\lambda = 0.70926$ Å.

2.5. High-temperature in situ laboratory XRD

High-temperature *in situ* XRD measurements were performed using a customized diffractometer equipped with a microfocus rotating anode (Mo $K\alpha_{1,2}$), a Pilatus 300 K-W area detector, and a home-built setup based on the design by Chupas *et al* [40, 41]. Specifically, the HEA-BM sample was sealed in a borosilicate glass capillary from Hilgenberg (0.48 mm inner diameter, 0.01 mm wall thickness) under Ar atmosphere and then inserted into a sapphire capillary of diameter 1.016 mm. Each pattern was collected for 75 s, and a heating rate of 1.4 °C min^{-1} was applied. Temperature control was accomplished using a thermocouple placed next to the capillary. Temperature calibration was done versus the cell volume of Al_2O_3 powder measured in a separate experiment [42].

2.6. Synchrotron XRD (SXRD) and total scattering

Measurements were performed with a photon energy of 60 keV ($\lambda = 0.2074$ Å) at beamline P02.1, PETRA III at Deutsches Elektronen-Synchrotron DESY in Hamburg, Germany [43]. Diffraction patterns were acquired using a VAREX XRD 4343CT 2D position-sensitive detector (150 × 150 μm^2 pixel size, 2880 × 2880 pixel area) at a sample-to-detector distance of 2200 and 300 mm for SXRD and total scattering, respectively. The exposure time for SXRD and total scattering was 60 and 600 s (i.e. 10 shots of 60 s duration), respectively. The total scattering data were merged using a Python script. Data calibration (LaB_6, NIST-660 c) and integration were done using the pyFAI software [44]. The PDFgetX3 software was applied to calculate G(r) from the raw total scattering data [45]. The data were first corrected for sample container contribution and Compton scattering, and then the normalized structure functions $S(Q)$ were obtained. Finally, $S(Q)$ was Fourier-transformed to yield $G(r)$ with $Q_{max} = 16$ $Å^{-1}$ and $r_{poly} = 1.2$ Å. The SXRD data were analyzed by Rietveld refinement using the FullProf Suite.

2.7. Time-of-flight (ToF) neutron powder diffraction (NPD)

For NPD, cylindrical vanadium containers of diameter 6 mm were filled with about 2 g of sample. Measurements were conducted at the Oak Ridge National Laboratory POWGEN beamline using a wavelength $\lambda = 1.5$ Å. The data were analyzed via Rietveld refinement using the FullProf Suite. The peak shape was modeled using the Thompson–Cox–Hastings pseudo-Voigt function, while a point-by-point background was subtracted. The parameters refined consecutively included the scale factor, peak shape parameters, lattice parameters, atomic coordinates, individual isotropic atomic displacement parameters, and lithium occupancies. The zero-shift parameter was refined last, and occupancies that resulted in unreasonable values were disregarded.

2.8. ^{6}Li, ^{29}Si, ^{31}P, and ^{119}Sn magic-angle spinning (MAS) nuclear magnetic resonance (NMR) spectroscopy

MAS NMR spectroscopy was performed at a magnetic field of 11.7 T, corresponding to resonance frequencies of 73.6, 99.4, 202.5, and 186.4 MHz for ^{6}Li, ^{29}Si, ^{31}P, and ^{119}Sn, respectively. Spinning was performed in 2.5 mm rotors at 20 kHz. Spectra were acquired with a single-pulse sequence for ^{6}Li, ^{29}Si, and ^{119}Sn, and with a Hahn-echo sequence for ^{31}P. The recycle delay was 60 s for ^{6}Li, ^{29}Si, and ^{31}P, and 30 s for ^{119}Sn. The $\pi/2$ pulse length was 2.9 μs for ^{6}Li, 3.3 μs for ^{29}Si, 2.7 μs for ^{31}P, and 1.8 μs for ^{119}Sn. The spectra were referenced to an aqueous 1 M ^{6}LiCl solution for ^{6}Li, tetramethylsilane for ^{29}Si, H_3PO_4 (85%) for ^{31}P, and SnO_2 for ^{119}Sn (−604.3 ppm) [46, 47].

2.9. Temperature-dependent ^{7}Li pulsed field gradient (PFG) NMR spectroscopy

Temperature-dependent ^{7}Li PFG NMR spectroscopy measurements were performed on a Bruker Avance spectrometer at a magnetic field of 7.05 T using a PFG probe of maximum gradient strength 30 T m^{-1}. The samples were investigated using a stimulated-echo-pulse sequence with bipolar gradients to suppress any effects of eddy currents [48]. The gradient duration was set to 3 ms, and diffusion times of 100 or 30 ms were chosen for HEA-BM, HEA-150, and HEA-220. The recycle delay was always well above five times the spin-lattice relaxation time. All samples were sealed in 5 mm evacuated borosilicate glass tubes.

2.10. Electrochemical impedance spectroscopy (EIS)

For conductivity measurements, about 200 mg of HEA-BM was compressed at 3.5 t for 3 min in a 10 mm diameter pellet die. The latter pellet was subjected to EIS measurements either without additional annealing or after annealing at 150 °C or 220 °C for 72 h. It was inserted into a customized setup with stainless steel dies and a 10 mm-diameter PEEK (polyether ether ketone) sleeve, and the electrochemical impedance was probed using an SP-200 potentiostat (BioLogic), from 0.1 Hz to 7 MHz with a 20 mV voltage amplitude and without applying external pressure. The spectra were collected from 15 °C to 65 °C after allowing for at least 1 h temperature equilibration prior to data collection. Spectra fitting was performed using an equivalent circuit model of type $RQ - W$ or $R_1Q_1 - R_2Q_2 - Q_3$, with R and Q being resistance and constant phase element, respectively. The conductivity was calculated from the total resistance, and the activation energy was obtained by Arrhenius fitting of the temperature-dependent conductivity. Residual porosity was not considered.

EIS measurements on SSB cells after cycling were performed under similar conditions. In this case, the spectra were fitted using an $R_1{-}R_2Q_2{-}R_3Q_3{-}R_4Q_4{-}Q_5$ equivalent circuit model, with R_1, R_2, R_3, and R_4 corresponding to the bulk, grain-boundary (GB), SE|CAM, and SE|AAM resistances, respectively.

2.11. Electrode preparation, cell assembly, and battery testing

The cathode composite was prepared by blending $LiNbO_3$-coated $LiNi_{0.85}Co_{0.1}Mn_{0.05}O_2$ (NCM851005, BASF SE) with the different SEs and Super C65 carbon black additive in a 69.3:29.7:1.0 weight ratio for 30 min at 140 rpm under Ar atmosphere using a 70 ml zirconia milling jar containing 10 zirconia balls of 10 mm in diameter. The protective coating on NCM851005 was prepared as reported previously [49]. For SSB assembly, a customized cell setup with two stainless steel dies and a 10 mm-diameter PEEK sleeve was used. First, about 100 mg of SE was pressed at 62.5 MPa to form the separator layer. Next, the cathode composite (∼13 mg) was spread onto the separator, followed by compressing the stack at 440 MPa. Both In/InLi and $Li_4Ti_5O_{12}$ (LTO) were tested as anodes. As for the former, an In disc (9 mm diameter, 125 μm thickness, Goodfellow) and a Li disc (6 mm diameter, 50 μm thickness, Albemarle Germany GmbH) were attached to the other side of the separator. The LTO anode composite was produced following the same ball-milling protocol as for the cathode composite. The weight ratio of carbon-coated LTO (NEI Corp.), Super C65, and SE was set to 30:10:60.

Galvanostatic charge/discharge measurements were performed under an external pressure of 81 MPa and at 45 °C, with C-rates ranging from 0.1 to 1 C (with 1 C = 190 mA/$g_{NCM851005}$), in the voltage windows of 2.28−3.68 V vs. In/InLi and 1.35−2.75 V vs. $Li_4Ti_5O_{12}/Li_7Ti_5O_{12}$ (equivalent to about 2.9−4.3 V vs. Li^+/Li; of note, potential differences with respect to Li^+/Li are ΔE = 0.62 V and ΔE = 1.55 V for In/InLi and $Li_4Ti_5O_{12}/Li_7Ti_5O_{12}$, respectively) after a resting period at open-circuit potential for 1 h using an MACCOR battery cycler.

3. Results and discussion

Different compositions were explored in an attempt to produce lithium argyrodites containing five different cationic substituents M in $Li_{6+a}MS_5I$ in equimolar fractions. Specifically, $Li_{6+a}[P_{0.2}Si_{0.2}Ge_{0.2}Sb_{0.2}M_{0.2}]S_5I$ materials with M = Sn, Ga, W, or Zn were targeted [12, 38]. To this end, the respective precursor mixtures were subjected to high-energy ball milling (figure 1(a)). As can be seen from the laboratory XRD patterns in figure S1, a phase-pure lithium argyrodite was only obtained for M = Sn. For the other cationic substituents tested in this work, distinct reflections related to Li_2S impurities can be clearly observed, even after 40 h of milling, indicating incomplete reactions. The chemical composition of the mechanochemically prepared $Li_{6.6}[P_{0.2}Si_{0.2}Sn_{0.2}Ge_{0.2}Sb_{0.2}]S_5I$ (HEA-BM) sample was confirmed by ICP-OES. The molar fractions of elements are given in table S1 and are in good agreement with the desired stoichiometry.

During the course of this work, we noticed that prolonged milling is necessary to ensure high phase purity. As evident from the XRD patterns in figure 1(b), the characteristic reflections of the argyrodite structure of HEA-BM are hardly visible after 10 h of milling. However, this changes with increasing milling duration. The relatively broad reflections and the diffuse background suggest the formation of a nanostructured material, as well as the presence of an amorphous side phase.

To assess if the degree of crystallinity can be increased by post-annealing, the HEA-BM sample was initially heated at 400 °C for 30 min or 10 h. Unfortunately, this led to decomposition of the argyrodite phase, as can be seen from the XRD patterns in figure S2. The onset temperature of undesired thermal decomposition was determined by high-temperature *in situ* XRD. The respective (stacked) patterns are shown in figure 1(c). Interestingly, the intensity of the (200) reflection located below 8° 2θ strongly increased at temperatures above 150 °C. For the other major reflections, namely (220) at >11° 2θ as well as (311) and (222) between 13° and 14° 2θ, the variations in intensity were less pronounced. However, for all reflections, the broadening decreased with increasing

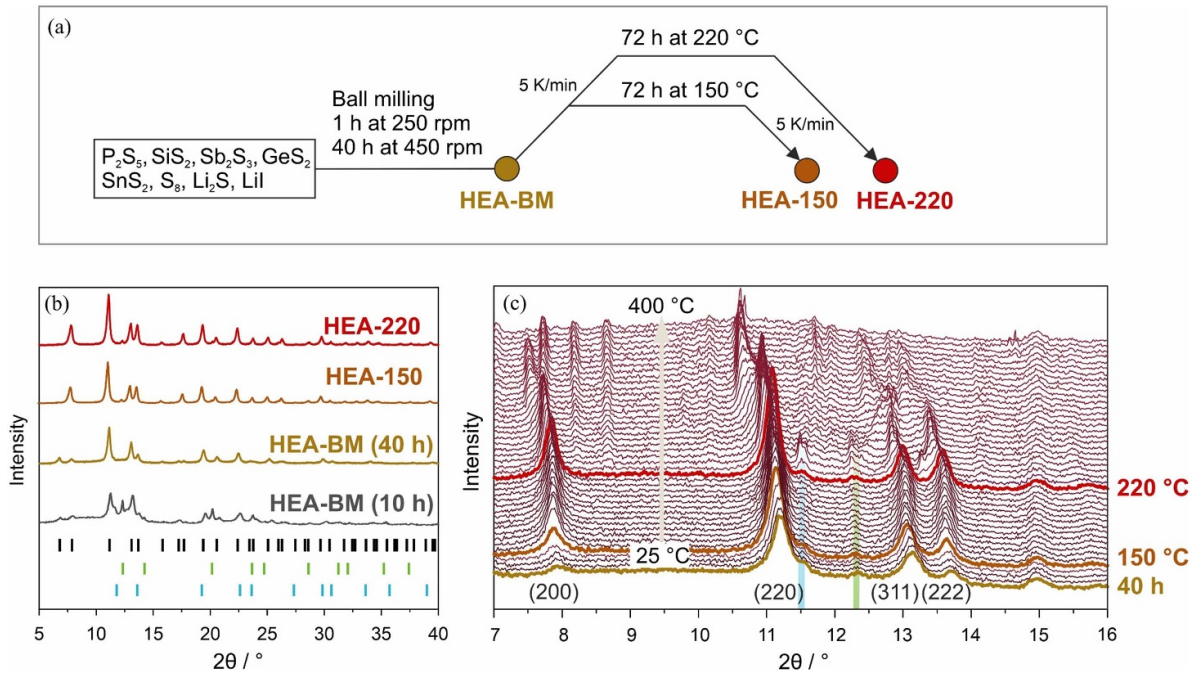

Figure 1. Synthetic exploration of the high-entropy lithium argyrodite $Li_{6.6}[P_{0.2}Si_{0.2}Sn_{0.2}Ge_{0.2}Sb_{0.2}]S_5I$. (a) Scheme for the preparation of samples tested in this work. (b) *Ex situ* XRD patterns collected from the precursor mixture after different ball-milling durations (HEA-BM) and the samples after post-annealing at 150 °C (HEA-150) and 220 °C (HEA-220). Vertical tick marks indicate the Bragg reflections for the argyrodite phase (black), Li_2S (green), and LiI (blue). (c) *In situ* XRD patterns of HEA-BM (40 h) upon heating from room temperature to 400 °C. Vertical bars indicate reflections for Li_2S (green) and LiI (blue).

temperature up to 220 °C, indicating improving crystallinity. Upon increasing the temperature beyond 220 °C, decomposition occurred, as indicated by the appearance of new reflections corresponding to LiI and Li_2S among other unknown impurity phases.

Based on the *in situ* XRD data, 150 °C and 220 °C were chosen as annealing temperatures. The corresponding samples are referred to as HEA-150 and HEA-220 hereafter. Thermal annealing was conducted on pelletized samples made from HEA-BM sealed in evacuated quartz ampules for 72 h, according to the synthesis scheme displayed in figure 1(a). Based on the initial observations made, it is apparent that $Li_{6.6}[P_{0.2}Si_{0.2}Sn_{0.2}Ge_{0.2}Sb_{0.2}]S_5I$ can be regarded as a metastable material, as it cannot be directly prepared from the binary precursors by high-temperature solid-state synthesis. Similar observations have been made in the past for Li_7GeS_5Br [50]. To confirm that no element segregation occurred upon annealing at 220 °C, high-angle annular dark-field STEM imaging and energy-dispersive x-ray spectroscopy mapping were performed. As shown in figure S3, the mapping results point toward uniform distribution of P, Si, Ge, Sb, and Sn at the submicrometer level.

To quantitatively determine the degree of crystallinity and gain structural insights, SXRD and ToF NPD measurements were conducted on the aforementioned materials. First, the HEA-BM, HEA-150, and HEA-220 samples were mixed with 20 wt.% silicon powder serving as an internal standard. The SXRD patterns and corresponding Rietveld profiles for HEA-BM and HEA-220 are presented in figures 2(a) and (b), respectively. The data for HEA-150 are shown in figure S4. All patterns could be indexed within the cubic $F\bar{4}3m$ space group, with a = 10.27357(4) Å for HEA-BM, 10.29073(7) Å for HEA-150, and 10.31917(1) Å for HEA-220. Detailed structural parameters are given in tables S2–S4. In comparison with the previously reported complex substituted $Li_{6.5}[P_{0.25}Si_{0.25}Ge_{0.25}Sb_{0.25}]S_5I$ with a = 10.29714(9) Å, the larger lattice parameter of HEA-220 suggests successful incorporation of Sn^{4+} into the lattice [12]. Conversely, the smaller lattice parameter found for the HEA-BM and HEA-150 samples is due to high S^{2-}/I^- site inversions of 55% and 39%, respectively, compared to only 10% for HEA-220. This kind of correlation between antisite defects and lattice parameter has already been reported in the literature [51–53].

As discussed above, thermal annealing strongly decreases the degree of site inversion (table S5). At the same time, the crystalline phase fraction increases from about 64 wt.% for HEA-BM to 94 wt.% for HEA-150 and 99 wt.% for HEA-220. However, the calculated crystallite size remains virtually unaltered (varying from 13 to 16 nm). Nevertheless, microstrain is strongly reduced from 50% for HEA-BM to 21% for HEA-220. Note that large microstrain is typically associated with high defect densities (e.g. vacancies, site disorder, etc) and poor crystallinity [54, 55]. Therefore, the lower microstrain after annealing can be attributed to both the lower S^{2-}/I^- site inversion and the higher degree of crystallinity.

Due to the low x-ray scattering cross-section of lithium and difficulties in precisely determining the S^{2-}/I^- site inversion, NPD measurements were also conducted on HEA-BM and

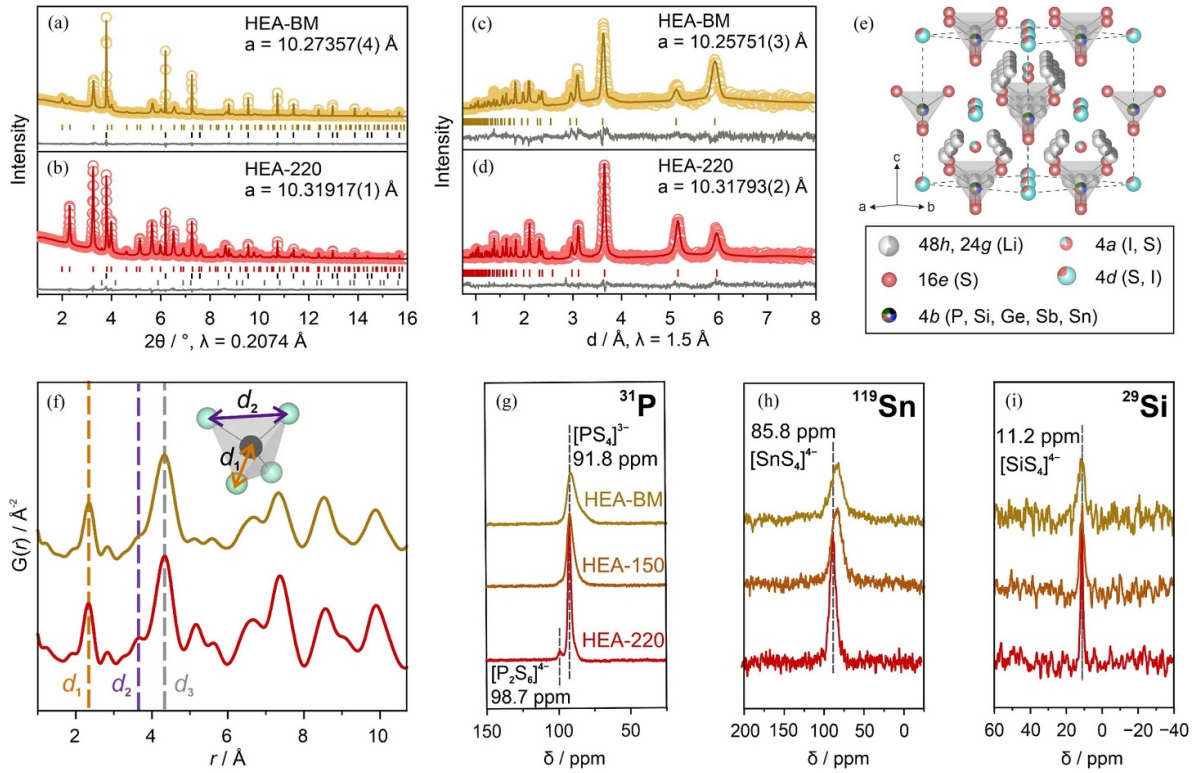

Figure 2. Structural characterization of the high-entropy lithium argyrodite $Li_{6.6}[P_{0.2}Si_{0.2}Sn_{0.2}Ge_{0.2}Sb_{0.2}]S_5I$. (a), (b) SXRD patterns collected from HEA-BM and HEA-220 in the presence of 20 wt.% Si standard reference material (NIST 640 f) and Rietveld plots. Open circles, dark yellow/red lines, and gray lines represent the measured, calculated, and difference data, respectively. Vertical tick marks indicate the anticipated Bragg positions: argyrodite (dark yellow/red), Si (black), and Li_2S (gray). (c), (d) Corresponding NPD patterns and Rietveld plots. (e) Crystal structure of HEA-220. (f) PDF curves for HEA-BM and HEA-220. (g)–(i) ^{31}P, ^{119}Sn, and ^{29}Si MAS NMR spectra of the different samples, as indicated.

HEA-220. The NPD patterns and corresponding Rietveld profiles are shown in figures 2(c) and (d), respectively. In general, similar lattice parameters were obtained (see tables S6 and S7 for details). As evident from table S8, the absolute value for the S^{2-}/I^{-} site inversion reaches 99% for HEA-BM and 10% for HEA-220, and a similar trend is observed for the microstrain (reducing from 81% to 31%). It should be noted that we were only able to fully refine the crystal structure of HEA-220. This is likely due to the relatively high fraction of amorphous side phase in the case of HEA-BM, causing significant diffuse scattering, as can be seen from the large background contribution present in the NPD pattern (figure 2(c)). A schematic representation of the calculated structure (for HEA-220) is shown in figure 2(e). Two Li positions were clearly identified, namely 48 h and 24 g. The latter allows us to calculate the configurational entropy, i.e. the occupational disorder, reaching $\Delta S_{conf} = 2.25$ R, which is among the highest values reported so far for lithium argyrodites and other lithium superionic conductors.

To probe the local structure of HEA-BM and HEA-220, synchrotron x-ray total scattering with pair distribution function (PDF) analysis was performed. As illustrated in figure 2(f), three contributions (d_1, d_2, and d_3) were identified. In particular, d_1 can be assigned to the (P/Si/Sn/Ge/Sb)−S covalent bonding within the tetrahedra and was determined to be about 2.33 Å for both samples. Similar values were also found for d_2 (S−S) = 3.66 Å and d_3 (S−S) = 4.33 Å, with d_2 referring to the S−S distance within the tetrahedra and d_3 denoting the distance to the next-neighboring tetrahedra. Overall, the bond lengths from the PDF analysis agree well with those determined by Rietveld refinements of the SXRD and NPD data.

To gain more insight into the (local) tetrahedral environments related to P, Si, and Sn, ^{31}P, ^{29}Si, and ^{119}Sn MAS NMR spectroscopy measurements were carried out. Clearly, all the spectra reveal similar trends (figures 2(g)−(i)). The broadest peaks are clearly visible for HEA-BM. As can be seen, the peak broadening (full width at half maximum, FWHM) is strongly decreased for the annealed samples. This is indicative of reduced local distortions, in line with the increase in crystallinity and decrease in microstrain discussed above. For the ^{31}P MAS NMR spectra (figure 2(g)), the major resonance is located at 91.8 ppm, representing isolated $[PS_4]^{3-}$ tetrahedra [12, 56–58]. The HEA-BM sample shows an additional broad shoulder toward lower chemical shifts. Deconvolution of the signal into broad and narrow contributions suggests the presence of a mixture of amorphous and crystalline phases (figure S5), thus corroborating the SXRD results. As expected, the intensity of the shoulder peak is strongly diminished for HEA-150, indicating a significantly lower contribution from the amorphous side phase (higher degree of crystallinity). For HEA-220, further narrowing of the main signal is obvious, with an additional minor peak appearing at 98.7 ppm. The latter ^{31}P peak is due to the formation of $[P_2S_6]^{4-}$ polyanions

Table 1. Summary of activation energy E_A and ionic conductivity σ_{ion} determined by temperature-dependent EIS and ^{7}Li PFG NMR spectroscopy (for HEA-220).

Sample	E_A (eV)	$\sigma_{ion,\ 25\ °C}$ (mS cm^{-1})
HEA-BM	0.36 ± 0.02	0.39 ± 0.17
HEA-150	0.35 ± 0.02	0.69 ± 0.09
HEA-220 (EIS)	0.32 ± 0.01	0.86 ± 0.11
HEA-220 (NMR)	0.27 ± 0.03	4.38 ± 0.21

[59, 60]. Collectively, the different spectra reveal two distinct contributions, which apparently can be correlated with the amorphous and crystalline phases present in the samples. Both the decrease in FWHM of the contribution assigned to the crystalline phase and the decrease in intensity of the contribution assigned to the amorphous phase upon annealing agree well with the relative increase in crystallinity determined by SXRD.

The ^{119}Sn spectra show a signal at a chemical shift of 83.5 ppm for HEA-BM (figure 2(h)), which increases to 85.8 ppm for HEA-220 (84.6 ppm for HEA-150). This suggests some changes in the local arrangement around the $[SnS_4]^{4-}$ polyanions and may be related to variations in the degree of S^{2-}/I^- site inversion. In contrast, the ^{29}Si spectra only exhibit a single peak centered at 11.2 ppm for the different samples (figure 2(i)). In general, the chemical shifts observed are consistent with the reported values for $[SnS_4]^{4-}$ and $[SiS_4]^{4-}$ polyanions [12, 61–63]. Moreover, ^{6}Li MAS NMR spectroscopy revealed a narrow peak at 1.43 ppm for HEA-BM, HEA-150, and HEA-220 (figure S6), characteristic of lithium argyrodites and indicating fast lithium mobility [64, 65].

The transport properties of cold-pressed pellets in the temperature range from 15 °C to 65 °C were probed using EIS. The corresponding Nyquist plots of the electrochemical impedance are presented in figure S7, while figure 3(a) shows the Arrhenius plots of the conductivity. The total room-temperature ionic conductivities are given in table 1, revealing an increase from 0.39 mS cm $^{-1}$ for HEA-BM to 0.86 mS cm $^{-1}$ for HEA-220. The lowest activation energy of $E_A = 0.32$ eV was found for HEA-220. A comparison between room-temperature ionic conductivity, S^{2-}/I^- site inversion, and crystallinity for the different samples is illustrated in figures 3(b) and (c). Typically, the conductivity of lithium argyrodite SEs exhibits a strong dependence on site inversion, with a high degree generally favoring high ionic conductivities [10, 12, 66]. At first glance, this relationship is not valid for the high-entropy glass–ceramic electrolytes employed here, as the site inversion decreases dramatically with increasing annealing temperature while the ionic conductivity increases. However, the increase in crystallinity (HEA-BM < HEA-150 < HEA-220) matches the trend seen in ionic conductivity. This result thus suggests that high crystallinity of compositionally complex lithium argyrodites is a prerequisite for achieving high ionic conductivity, and amorphous side phase(s) are disadvantageous.

Recently, Sadowski *et al* reported on the relationship between lattice structure (site inversion), microstructure (grain boundaries), and ionic conductivity in Li_6PS_5Br [67]. They revealed that a low degree of site inversion tends to hinder bulk diffusion but enhances GB conductivity, whereas a high degree leads to opposite effects. Therefore, the aforementioned structural characteristics seem to simultaneously affect lithium mobility. The high site inversion observed for HEA-BM may be detrimental to the GB diffusion while exerting a positive effect on bulk diffusion. Although HEA-150 and HEA-220 have a much higher crystallinity than HEA-BM, the domain sizes remain small (table S5), meaning the density of GBs is high. With the site inversion decreasing from HEA-BM to HEA-220, GB diffusion may be facilitated; however, the overall conductivity is adversely affected by unfavorable bulk diffusion.

To further examine the lithium diffusion, ^{7}Li PFG NMR spectroscopy was performed in the temperature range from 29 to 65 °C. The temperature-dependent echo intensity of HEA-BM plotted as $\ln(I)$ against g^2 (squared gradient strength) is displayed in figure 3(d). As can be seen, data analysis requires two-component fitting. For a single diffusion coefficient, plotting $\ln(I)$ versus g^2 results in a straight line according to the equation given by Stejskal and Tanner:

$$I = I_0 \cdot \exp\left(-D\gamma^2\delta^2 g^2\left(\Delta - \frac{\delta}{3}\right)\right).$$

Here, δ describes the gradient pulse duration, Δ the diffusion time, D the diffusion coefficient for lithium, and γ represents the magnetogyric ratio [68]. However, the slope of $\ln(I)$ was found to change with increasing g^2 for all samples (figures 3(d) and S8), thereby clearly indicating the presence of a second diffusion coefficient. In this case of two independent diffusion coefficients, the damping of echo intensity $I(g)$ is given by the sum of contributions according to the aforementioned equation, where δ, Δ, and γ are equal. The fit with $I(g) = \sum_i I_i$ yields the diffusion coefficients D_i as well as the relative amplitudes $I_{0,i}$. The latter can be differently affected by the spin-spin and spin-lattice relaxation times and therefore provides only an estimate of the real phase fractions that are characterized by D_i. To exclude the influence of experimental parameters, different diffusion times of 100 and 30 ms were considered. Here, the need for two-component data fitting was also observed, demonstrating that this characteristic can indeed be attributed to the samples under study. Note that similar observations have been made for other lithium thiophosphates too [69, 70]. Arrhenius plots of the lithium diffusion coefficient D_{Li} from ^{7}Li PFG NMR spectroscopy for HEA-BM, HEA-150, and HEA-220, measured with a diffusion time of 100 ms, are shown in figure 3(e). The higher (solid lines) and lower D_{Li} (dashed lines) refer to the major and minor components, respectively. The existence of two diffusion coefficients (and their dependence on the synthetic conditions) can be explained by the presence of crystalline (major) and amorphous phases (minor), as detailed above. The signal contribution of the minor component is found to decrease with increasing annealing temperature. Hence, we hypothesize that the D_{Li} of the major component describes the diffusion within the nanocrystalline phase. In particular, the virtual disappearance

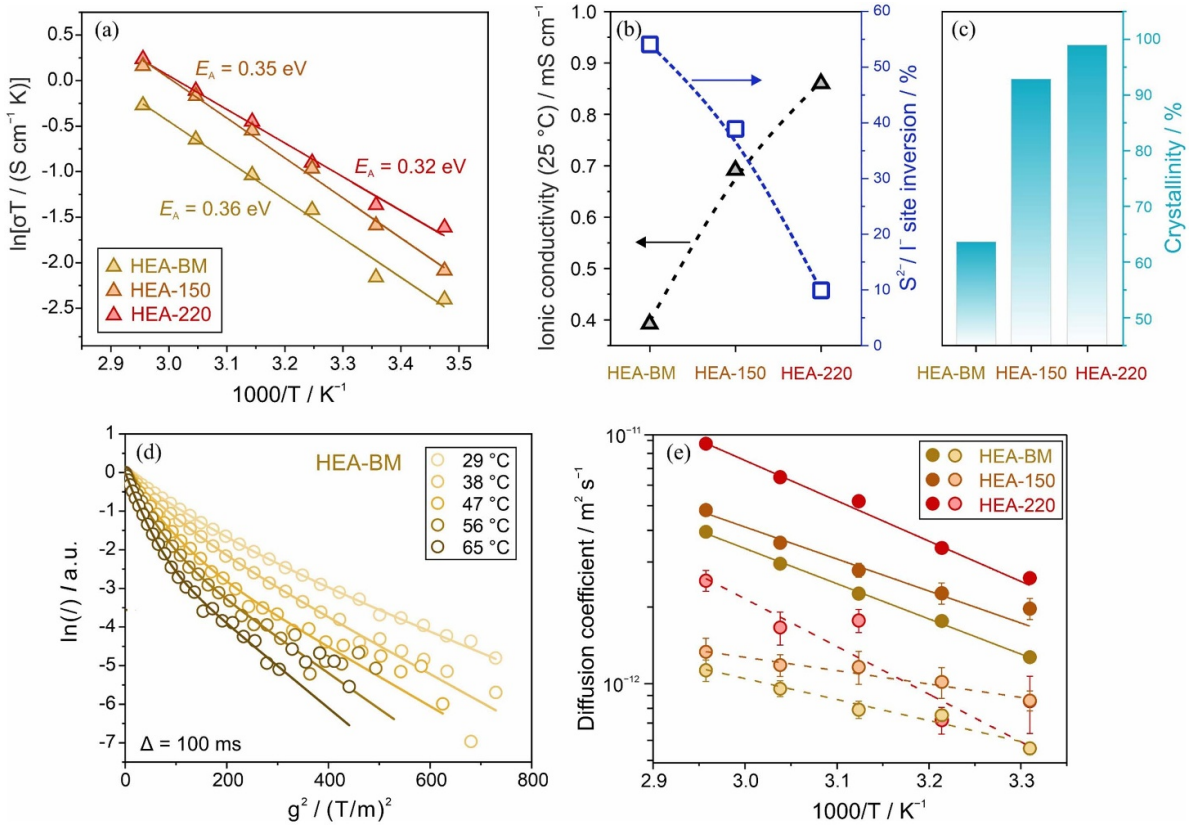

Figure 3. (a) Arrhenius plots of the conductivity determined by EIS. Activation energies are indicated. (b) Comparison between ionic conductivity measured on cold-pressed pellets via EIS at 25 °C, S^{2-}/I^- site inversion, and (c) degree of crystallinity for HEA-BM, HEA-150, and HEA-220. (d) Temperature-dependent echo intensity of HEA-BM plotted as ln(I) against squared gradient strength and (e) Arrhenius plots of the lithium diffusion coefficient determined by ^{7}Li PFG NMR spectroscopy with a diffusion time of 100 ms.

of the minor component in the HEA-220 sample hints at a negligible fraction of the amorphous side phase, in agreement with the SXRD results. Also, as evident from figure S9, a change in Δ hardly affects the activation energy and diffusion coefficient of the major component, whereas a much stronger effect is observed for the minor component. The results for E_A, D_{Li}, and σ_{ion} are given in table S9. In general, the D_{Li} of the major and minor components increases with increasing annealing temperature. In particular, for HEA-220, the D_{Li} of the major component was determined to be about $(2.54 \pm 0.05) \times 10^{-12}$ m^2 s^{-1} at 29 °C, which is comparable to that of other lithium thiophosphate superionic conductors (e.g. $D_{Li,\,30\,°C} = 2.5 \times 10^{-12}$ m^2 s^{-1} for Li_6PS_5Cl). As the HEA-220 sample is largely devoid of amorphous side phases, the ionic conductivity can be calculated from the D_{Li} using the Nernst–Einstein equation (under consideration of the crystal structure in figure 2(e)). This leads to a bulk ionic conductivity of about 4.4 mS cm^{-1}, much higher than that determined by EIS (table 1), and implies that impurities or surface residuals impede macroscopic ion transport through the material. These trace impurities cannot be detected by diffraction techniques. However, they appear in the form of tiny peaks in the ^{31}P MAS NMR spectra (figure 2(g)) and likely account for the diminished ionic conductivity [71].

Finally, the electrochemical behavior of HEA-BM and HEA-220 as SEs was examined in pellet-stack SSB cells with a $LiNbO_3$-coated $LiNi_{0.85}Co_{0.1}Mn_{0.05}O_2$ (NCM851005) cathode and an In/InLi anode. Commercially available argyrodite Li_6PS_5Cl was also tested for comparison. The cells were initially charged and discharged at a rate of C/10 and at 45 °C. The first-cycle voltage profiles are presented in figure 4(a). Specifically, specific charge capacities of 234, 236, and 218 mAh g^{-1} were achieved with HEA-BM, HEA-220, and Li_6PS_5Cl, respectively. The corresponding specific discharge capacities are 205, 201, and 194 mAh g^{-1}, translating to initial Coulomb efficiencies of 88%, 85%, and 89% (figure 4(b)). Compared to the $Li_{6.5}[P_{0.25}Si_{0.25}Ge_{0.25}Sb_{0.25}]S_5I$ SE tested previously under similar conditions, the Coulomb efficiency in the first cycle was significantly improved, by about 10%, for $Li_{6.6}[P_{0.2}Si_{0.2}Sn_{0.2}Ge_{0.2}Sb_{0.2}]S_5I$. This is due in part to the lower fraction of 'unfavorable' elemental constituents (i.e. Sb and Si) [12, 72]. After two formation cycles at C/10, the SSBs were subjected to rate performance testing (figure 4(c)). Cells with HEA-BM and HEA-220 delivered specific discharge capacities of 189 and 162 mAh g^{-1} at C/5, 158 and 125 mAh g^{-1} at C/2, and 126 and 91 mAh g^{-1} at 1 C, respectively (figure 4(d)). Using Li_6PS_5Cl, specific discharge capacities of 180, 158, and 136 mAh g^{-1} were achieved at C/5, C/2, and 1 C, respectively. The higher capacity of the Li_6PS_5Cl-based cells at C-rates $\geqslant$ 1 C (1 C $\approx$ 2.5 mA cm^{-2}) can be attributed to the higher ionic conductivity of Li_6PS_5Cl, ~8 mS cm^{-1} at 45 °C compared to ~3 mS cm^{-1} for the

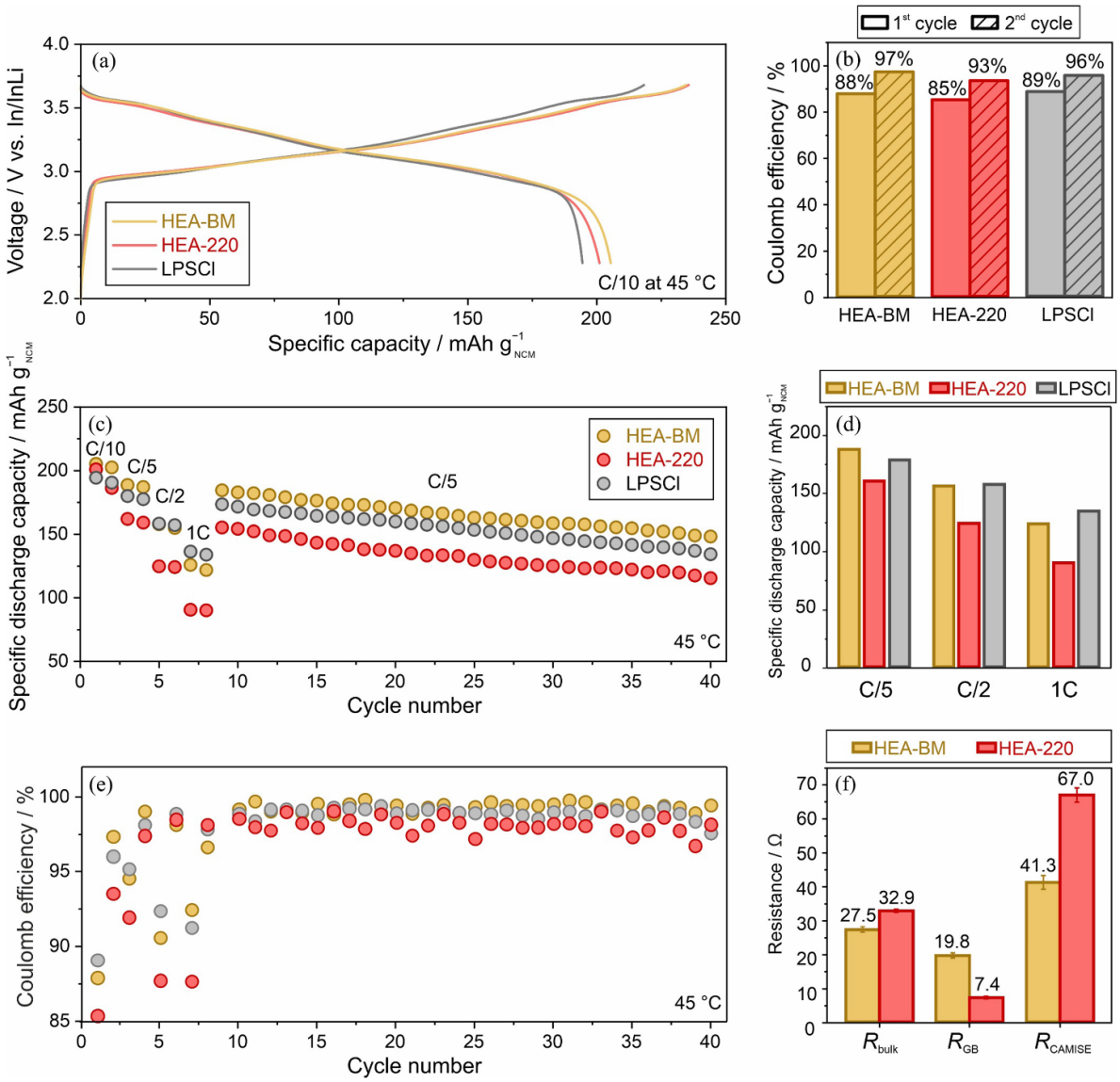

Figure 4. (a) Initial voltage profiles of SSB cells using either HEA-BM, HEA-220, or Li_6PS_5Cl as SEs at C/10 rate and at 45 °C and (b) first- and second-cycle Coulomb efficiencies. (c) Rate capability and long-term cycling performance at C/5. (d) Specific discharge capacities achieved at C/5, C/2, and 1 C in the rate performance testing. (e) Coulomb efficiencies for the first 40 cycles. (f) Individual resistances determined by fitting EIS data collected from the cells after 66 cycles.

HEA SEs. Subsequently, the SSBs were cycled at C/5, revealing fairly linear fading rates for the different materials tested. Regardless, the cells using HEA-BM and HEA-220 were still capable of delivering specific discharge capacities of 148 and 115 mAh g^{-1}, respectively, after 40 cycles. Although the initial Coulomb efficiency was similar for both SEs, those achieved with HEA-BM were highest during prolonged cycling (figure 4(e)). They were found to stabilize below 99% for HEA-220 and above 99% for both HEA-BM and Li_6PS_5Cl.

The electrochemical performance of SSBs using zero-strain LTO as an anode active material was also examined for HEA-BM and HEA-220. Similar to the In/InLi case, cells with HEA-BM delivered higher specific capacities than those with HEA-220, irrespective of the C-rate (figure S10).

Finally, *ex situ* EIS measurements were conducted on the LTO-based cells after 66 cycles. Nyquist plots of the electrochemical impedance, along with simulated data, are presented in figure S10. Individual resistances were determined for the bulk SE (R_{bulk}), grain boundary (R_{GB}), and cathode and anode interface ($R_{CAM|SE}$ and $R_{AAM|SE}$, respectively) contributions (see tables S10 and S11 for details). Because the (electro)chemical degradation occurring at the CAM|SE interface is responsible, to some extent, for the performance decline upon cycling and in line with expectations, a smaller resistance of $R_{CAM|SE} \approx 41\ \Omega$ was observed for HEA-BM, compared to $\sim$67 Ω for HEA-220 (figure 4(f)). However, the data demonstrate that degradation at both the positive and negative electrode sides is driving capacity fading.

Aside from (electro)chemically driven degradation reactions, mechanical processes play a major role too [73]. This is primarily due to the large volume changes that Ni-rich CAMs undergo during battery operation, which may lead to contact loss between the CAM and SE particles and crack formation, both negatively interfering with performance [74]. In

this regard, our study points toward the benefits of employing glass–ceramic SEs in maintaining proper contact among the cathode particles. Despite the fact that the ionic conductivity of HEA-BM was lower than that of HEA-220, the SSB performance was much improved for the former, indicating that not only transport but also mechanical properties of SEs need to be considered in designing advanced electrodes, with glass–ceramics offering more freedom for tailoring to specific requirements.

4. Conclusions

In summary, we have successfully synthesized a high-entropy argyrodite SE of nominal composition $Li_{6.6}[P_{0.2}Si_{0.2}Sn_{0.2}Ge_{0.2}Sb_{0.2}]S_5I$, with the mechanochemistry approach employed leading to the formation of a glass–ceramic. As expected, the crystallinity can be increased by annealing, which also reduces the density of S^{2-}/I^- antisite defects. Complementary electrochemical impedance and ^{7}Li PFG NMR spectroscopy measurements indicate that the crystallinity positively affects ionic conductivity, leading to a total conductivity of about 0.9 mS cm^{-1} (∼4.4 mS cm^{-1} bulk conductivity) at room temperature after annealing at 220 °C. The SE in the pristine state (64% crystallinity) and after post-treatment (99% crystallinity) was further tested in pelletized SSBs, with commercially available Li_6PS_5Cl serving as a reference (baseline) material. Notably, cells with the glass–ceramic electrolyte exhibit much improved cycling performance over those using either the annealed material or Li_6PS_5Cl, likely due to better contact with the layered Ni-rich oxide CAM and more favorable chemomechanical behavior upon battery operation. Taken together, our data indicate (i) the importance of considering microstructure as well as chemical and phase composition of lithium argyrodite SEs when tailoring their properties toward battery applications and (ii) the great potential that lies in compositionally complex glass–ceramic ion conductors.

5. Future perspectives

The need for advanced batteries, especially for the e-mobility sector, has strongly accelerated the development of solid-state battery technology. To make it competitive with conventional Li-ion batteries using liquid electrolytes, advanced SEs are needed. The latter materials must exhibit a high room-temperature ionic conductivity while being (electro)chemically stable and mechanically soft. However, designing soft, inorganic SEs represents a major challenge. Among the existing classes of superionic SEs, glass–ceramics offer favorable properties in this regard. In particular, tailoring chemical and phase composition provides ample opportunities for improving their properties.

Acknowledgment

F S is grateful to the Federal Ministry of Education and Research (BMBF) for funding within the project MELLi (03XP0447). This work was partially supported by BASF SE. A portion of this research used resources at the Spallation Neutron Source, a DOE Office of Science User Facility operated by the Oak Ridge National Laboratory. The beamtime was allocated to POWGEN on proposal number IPTS-29027. We acknowledge DESY (Hamburg, Germany), a member of the Helmholtz Association HGF, for the provision of experimental facilities. Parts of this research were carried out at PETRA III, beamline P02.1. Beamtime was allocated for proposal 11016067. The authors thank Leonhard Karger (KIT) and Thomas Bergfeldt (KIT) for help in collecting the high-temperature *in situ* XRD and ICP-OES data, respectively.

Conflict of interest

The authors declare the following interest(s): a patent was filed for this work through BASF SE and Karlsruher Institut für Technologie (KIT).

Authors contribution

The experiments were planned and designed by the first author under the supervision of Torsten Brezesinski and Florian Strauss. Jing Lin developed and optimized the synthesis method. The NPD measurements were performed at the Spallation Neutron Source operated by Oak Ridge National Laboratory, and the data collected was analyzed by Jing Lin. The SXRD measurements were performed at PETRA III, DESY, with the assistance from Volodymyr Baran and Hao Liu, and the data collected was analyzed by Jing Lin. Jing Lin also performed the EIS and GCPL measurements and analyzed the corresponding data. Mareen Schaller performed the ^{7}Li PFG NMR spectroscopy measurements and analyzed the data together with Jing Lin. Sylvio Indris performed the MAS NMR spectroscopy measurements and analyzed the data. Ziming Ding conducted the (S)TEM investigation. Ruizhuo Zhang conducted the EIS analysis. The first draft was written by Jing Lin. Torsten Brezesinski and Florian Strauss provided guidance during the revision process. The final paper was edited by all co-authors.

ORCID iDs

Jing Lin https://orcid.org/0000-0002-6403-4803
Mareen Schaller https://orcid.org/0000-0001-6589-2087
Volodymyr Baran https://orcid.org/0000-0003-2379-3632
Sylvio Indris https://orcid.org/0000-0002-5100-113X
Torsten Brezesinski https://orcid.org/0000-0002-4336-263X
Florian Strauss https://orcid.org/0000-0001-5817-6349

References

[1] Janek J and Zeier W G 2016 A solid future for battery development *Nat. Energy* **1** 16141
[2] Frith J T, Lacey M J and Ulissi U 2023 A non-academic perspective on the future of lithium-based batteries *Nat. Commun.* **14** 420

[3] Kim K J, Balaish M, Wadaguchi M, Kong L and Rupp J L M 2021 Solid-state Li–metal batteries: challenges and horizons of oxide and sulfide solid electrolytes and their interfaces *Adv. Energy Mater.* **11** 2002689

[4] Zhang Z *et al* 2018 New horizons for inorganic solid state ion conductors *Energy Environ. Sci.* **11** 1945–76

[5] Janek J and Zeier W G 2023 Challenges in speeding up solid-state battery development *Nat. Energy* **8** 230–40

[6] Bachman J C *et al* 2016 Inorganic solid-state electrolytes for lithium batteries: mechanisms and properties governing ion conduction *Chem. Rev.* **116** 140–62

[7] Famprikis T, Canepa P, Dawson J A, Islam M S and Masquelier C 2019 Fundamentals of inorganic solid-state electrolytes for batteries *Nat. Mater.* **18** 1278–91

[8] Minafra N, Kraft M A, Bernges T, Li C, Schlem R, Morgan B J and Zeier W G 2020 Local charge inhomogeneity and lithium distribution in the superionic argyrodites Li_6PS_5X (X = Cl,Br,I) *Inorg. Chem.* **59** 11009–19

[9] Kraft M A, Culver S P, Calderon M, Böcher F, Krauskopf T, Senyshyn A, Dietrich C, Zevalkink A, Janek J and Zeier W G 2017 Influence of lattice polarizability on the ionic conductivity in the lithium superionic argyrodites Li_6PS_5X (X = Cl, Br, I) *J. Am. Chem. Soc.* **139** 10909–18

[10] Kraft M A, Ohno S, Zinkevich T, Koerver R, Culver S P, Fuchs T, Senyshyn A, Indris S, Morgan B J and Zeier W G 2018 Inducing high ionic conductivity in the lithium superionic argyrodites $Li_{6+x}P_{1-x}Ge_xS_5I$ for all-solid-state batteries *J. Am. Chem. Soc.* **140** 16330–9

[11] Ohno S, Helm B, Fuchs T, Dewald G, Kraft M A, Culver S P, Senyshyn A and Zeier W G 2019 Further evidence for energy landscape flattening in the superionic argyrodites $Li_{6+x}P_{1-x}M_xS_5I$ (M = Si, Ge, Sn) *Chem. Mater.* **31** 4936–44

[12] Lin J, Cherkashinin G, Schäfer M, Melinte G, Indris S, Kondrakov A, Janek J, Brezesinski T and Strauss F 2022 A high-entropy multicationic substituted lithium argyrodite superionic solid electrolyte *ACS Mater. Lett.* **4** 2187–94

[13] Zhao Y, Li J and Dahn J R 2017 Interdiffusion of cations from metal oxide surface coatings into $LiCoO_2$ during sintering *Chem. Mater.* **29** 5239–48

[14] Brinek M, Hiebl C and Wilkening H M R 2020 Understanding the origin of enhanced Li-ion transport in nanocrystalline argyrodite-type Li_6PS_5I *Chem. Mater.* **32** 4754–66

[15] Teo J H, Strauss F, Walther F, Ma Y, Payandeh S, Scherer T, Bianchini M, Janek J and Brezesinski T 2022 The interplay between (electro)chemical and (chemo)mechanical effects in the cycling performance of thiophosphate-based solid-state batteries *Mater. Futures* **1** 015102

[16] Strauss F, Teo J H, Janek J and Brezesinski T 2020 Investigations into the superionic glass phase of Li_4PS_4I for improving the stability of high-loading all-solid-state batteries *Inorg. Chem. Front.* **7** 3953–60

[17] Strauss F, Lin J, Karger L, Weber D and Brezesinski T 2022 Probing the lithium substructure and ionic conductivity of the solid electrolyte Li_4PS_4I *Inorg. Chem.* **61** 5885–90

[18] Jodlbauer A, Spychala J, Hogrefe K, Gadermaier B and Wilkening H M R 2024 Fast Li ion dynamics in defect-rich nanocrystalline Li_4PS_4I—the effect of disorder on activation energies and attempt frequencies *Chem. Mater.* **36** 1648–64

[19] Miß V *et al* 2022 Heat treatment-induced conductivity enhancement in sulfide-based solid electrolytes: what is the role of the Thio-LISICON II phase and of other nanoscale phases? *Chem. Mater.* **34** 7721–9

[20] Brandstätter H, Wohlmuth D, Bottke P, Pregartner V and Wilkening M 2015 Li ion dynamics in nanocrystalline and structurally disordered Li_2TiO_3 *Z. Phys. Chem.* **229** 1363–74

[21] Heitjans P, Masoud M, Feldhoff A and Wilkening M 2007 NMR and impedance studies of nanocrystalline and amorphous ion conductors: lithium niobate as a model system *Faraday Discuss.* **134** 67–82

[22] Liu Z, Fu W, Payzant E A, Yu X, Wu Z, Dudney N J, Kiggans J, Hong K, Rondinone A J and Liang C 2013 Anomalous high ionic conductivity of nanoporous β-Li_3PS_4 *J. Am. Chem. Soc.* **135** 975–8

[23] Strauss F, Lin J, Janek J and Brezesinski T 2021 Influence of synthesis parameters on crystallization behavior and ionic conductivity of the Li_4PS_4I solid electrolyte *Sci. Rep.* **11** 14073

[24] Di Stefano D *et al* 2019 Superionic diffusion through frustrated energy landscape *Chem* **5** 2450–60

[25] Schweiger L, Hogrefe K, Gadermaier B, Rupp J L M and Wilkening M 2022 Ionic conductivity of nanocrystalline and amorphous $Li_{10}GeP_2S_{12}$: the detrimental impact of local disorder on ion transport *J. Am. Chem. Soc.* **144** 9597–609

[26] Yang J, Lin J, Brezesinski T and Strauss F 2024 Emerging superionic sulfide and halide glass-ceramic solid electrolytes: recent progress and future perspectives *ACS Energy Lett.* **9** 5977–90

[27] Singh D K, Henss A, Mogwitz B, Gautam A, Horn J, Krauskopf T, Burkhardt S, Sann J, Richter F H and Janek J 2022 Li_6PS_5Cl microstructure and influence on dendrite growth in solid-state batteries with lithium metal anode *Cell Rep. Phys. Sci.* **3** 101043

[28] Singh D K, Fuchs T, Krempaszky C, Mogwitz B and Janek J 2023 Non-linear kinetics of the lithium metal anode on Li_6PS_5Cl at high current density: dendrite growth and the role of lithium microstructure on creep *Adv. Sci.* **10** 2302521

[29] Wang S *et al* 2021 Influence of crystallinity of lithium thiophosphate solid electrolytes on the performance of solid-state batteries *Adv. Energy Mater.* **11** 2100654

[30] Schweidler S *et al* 2024 High-entropy materials for energy and electronic applications *Nat. Rev. Mater.* **9** 266–81

[31] Oses C, Toher C and Curtarolo S 2020 High-entropy ceramics *Nat. Rev. Mater.* **5** 295–309

[32] Ma Y, Ma Y, Wang Q, Schweidler S, Botros M, Fu T, Hahn H, Brezesinski T and Breitung B 2021 High-entropy energy materials: challenges and new opportunities *Energy Environ. Sci.* **14** 2883–905

[33] Zeng Y, Ouyang B, Liu J, Byeon Y-W, Cai Z, Miara L J, Wang Y and Ceder G 2022 High-entropy mechanism to boost ionic conductivity *Science* **378** 1320–4

[34] Fan J *et al* 2023 Entropy stabilized cubic $Li_7La_3Zr_2O_{12}$ with reduced lithium diffusion activation energy: studied using solid-state NMR spectroscopy *RSC Adv.* **13** 19856–61

[35] Jung S-K, Gwon H, Kim H, Yoon G, Shin D, Hong J, Jung C and Kim J-S 2022 Unlocking the hidden chemical space in cubic-phase garnet solid electrolyte for efficient quasi-all-solid-state lithium batteries *Nat. Commun.* **13** 7638

[36] Ko S-T *et al* 2023 Compositionally complex perovskite oxides: discovering a new class of solid electrolytes with interface-enabled conductivity improvements *Matter* **6** 2395–418

[37] Li Y *et al* 2023 A lithium superionic conductor for millimeter-thick battery electrode *Science* **381** 50–53

[38] Lin J, Schaller M, Indris S, Baran V, Gautam A, Janek J, Kondrakov A, Brezesinski T and Strauss F 2024 Tuning ion mobility in lithium argyrodite solid electrolytes via entropy engineering *Angew. Chem., Int. Ed.* **63** e202404874

[39] Li S, Lin J, Schaller M, Indris S, Zhang X, Brezesinski T, Nan C-W, Wang S and Strauss F 2023 High-entropy lithium argyrodite solid electrolytes enabling stable all-solid-state batteries *Angew. Chem., Int. Ed.* **62** e202314155

[40] Chupas P J, Chapman K W, Kurtz C, Hanson J C, Lee P L and Grey C P 2008 A versatile sample-environment cell for

non-ambient x-ray scattering experiments *J. Appl. Crystallogr.* **41** 822–4
[41] de Biasi L *et al* 2015 Unravelling the mechanism of lithium insertion into and extraction from trirutile-type $LiNiFeF_6$ cathode material for Li-ion batteries *CrystEngComm* **17** 6163–74
[42] Stinton G W and Evans J S O 2007 Parametric rietveld refinement *J. Appl. Crystallogr.* **40** 87–95
[43] Dippel A-C, Liermann H-P, Delitz J T, Walter P, Schulte-Schrepping H, Seeck O H and Franz H 2015 Beamline P02.1 at PETRA III for high-resolution and high-energy powder diffraction *J. Synchrotron Radiat.* **22** 675–87
[44] Ashiotis G, Deschildre A, Nawaz Z, Wright J P, Karkoulis D, Picca F E and Kieffer J 2015 The fast azimuthal integration python library: pyFAI *J. Appl. Crystallogr.* **48** 510–9
[45] Juhás P, Davis T, Farrow C L and Billinge S J L 2013 PDFgetX3: a rapid and highly automatable program for processing powder diffraction data into total scattering pair distribution functions *J. Appl. Crystallogr.* **46** 560–6
[46] Clayden N J, Dobson C M and Fern A 1989 High-resolution solid-state tin-119 nuclear magnetic resonance spectroscopy of ternary tin oxides *J. Chem. Soc., Dalton Trans.* **5** 843–7
[47] Cossement C, Darville J, Gilles J-M, Nagy J B, Fernandez C and Amoureux J-P 1992 Chemical shift anisotropy and indirect coupling in SnO_2 and SnO *Magn. Reson. Chem.* **30** 263–70
[48] Price W S 1998 Pulsed-field gradient nuclear magnetic resonance as a tool for studying translational diffusion: part II. Experimental aspects *Concepts Magn. Reson.* **10** 197–237
[49] Payandeh S, Strauss F, Mazilkin A, Kondrakov A and Brezesinski T 2022 Tailoring the $LiNbO_3$ coating of Ni-rich cathode materials for stable and high-performance all-solid-state batteries *Nano Res. Energy* **1** 9120016
[50] Strauss F, Zinkevich T, Indris S and Brezesinski T 2020 Li_7GeS_5Br-An argyrodite Li-ion conductor prepared by mechanochemical synthesis *Inorg. Chem.* **59** 12954–9
[51] Gautam A, Sadowski M, Ghidiu M, Minafra N, Senyshyn A, Albe K and Zeier W G 2021 Engineering the site-disorder and lithium distribution in the lithium superionic argyrodite Li_6PS_5Br *Adv. Energy Mater.* **11** 2003369
[52] Gautam A *et al* 2019 Rapid crystallization and kinetic freezing of site-disorder in the lithium superionic argyrodite Li_6PS_5Br *Chem. Mater.* **31** 10178–85
[53] Park S and Lee J-W 2021 Structure and ion conductivity study of argyrodite ($Li_{5.5}PS_{4.5}Cl_{1.5}$) according to cooling method *J. Korean Inst. Met. Mater.* **59** 247–55
[54] Banik A, Famprikis T, Ghidiu M, Ohno S, Kraft M A and Zeier W G 2021 On the underestimated influence of synthetic conditions in solid ionic conductors *Chem. Sci.* **12** 6238–63
[55] Rodríguez-Carvajal J 1993 Recent advances in magnetic structure determination by neutron powder diffraction *Physica B* **192** 55–69
[56] Stöffler H *et al* 2019 Amorphous versus crystalline Li_3PS_4: local structural changes during synthesis and Li ion mobility *J. Phys. Chem. C* **123** 10280–90
[57] Liu Z, Zinkevich T, Indris S, He X, Liu J, Xu W, Bai J, Xiong S, Mo Y and Chen H 2020 $Li_{15}P_4S_{16}Cl_3$, a lithium chlorothiophosphate as a solid-state ionic conductor *Inorg. Chem.* **59** 226–34
[58] Strauss F, Lin J, Duffiet M, Wang K, Zinkevich T, Hansen A-L, Indris S and Brezesinski T 2022 High-entropy polyanionic lithium superionic conductors *ACS Mater. Lett.* **4** 418–23
[59] Dietrich C, Sadowski M, Sicolo S, Weber D A, Sedlmaier S J, Weldert K S, Indris S, Albe K, Janek J and Zeier W G 2016 Local structural investigations, defect formation, and ionic conductivity of the lithium ionic conductor $Li_4P_2S_6$ *Chem. Mater.* **28** 8764–73
[60] Dietrich C, Weber D A, Sedlmaier S J, Indris S, Culver S P, Walter D, Janek J and Zeier W G 2017 Lithium ion conductivity in Li_2S-P_2S_5 glasses-building units and local structure evolution during the crystallization of superionic conductors Li_3PS_4, $Li_7P_3S_{11}$ and $Li_4P_2S_7$ *J. Mater. Chem. A* **5** 18111–9
[61] Kaus M, Stöffler H, Yavuz M, Zinkevich T, Knapp M, Ehrenberg H and Indris S 2017 Local structures and Li ion dynamics in a $Li_{10}SnP_2S_{12}$-based composite observed by multinuclear solid-state NMR spectroscopy *J. Phys. Chem. C* **121** 23370–6
[62] Hartmann F, Benkada A, Indris S, Poschmann M, Lühmann H, Duchstein P, Zahn D and Bensch W 2022 Directed dehydration as synthetic tool for generation of a new Na_4SnS_4 polymorph: crystal structure, Na^+ conductivity, and influence of Sb-substitution *Angew. Chem., Int. Ed.* **61** e202202182
[63] Harm S, Hatz A-K, Moudrakovski I, Eger R, Kuhn A, Hoch C and Lotsch B 2019 Lesson learned from NMR: characterization and ionic conductivity of LGPS-like Li_7SiPS_8 *Chem. Mater.* **31** 1280–8
[64] Schlenker R, Hansen A-L, Senyshyn A, Zinkevich T, Knapp M, Hupfer T, Ehrenberg H and Indris S 2020 Structure and diffusion pathways in Li_6PS_5Cl argyrodite from neutron diffraction, pair-distribution function analysis, and NMR *Chem. Mater.* **32** 8420–30
[65] Hogrefe K, Minafra N, Hanghofer I, Banik A, Zeier W G and Wilkening H M 2022 Opening diffusion pathways through site disorder: the interplay of local structure and ion dynamics in the solid electrolyte $Li_{6+x}P_{1-x}Ge_xS_5I$ as probed by neutron diffraction and NMR *J. Am. Chem. Soc.* **144** 1795–812
[66] Zhou L, Minafra N, Zeier W G and Nazar L 2021 Innovative approaches to Li-argyrodite solid electrolytes for all-solid-state lithium batteries *Acc. Chem. Res.* **54** 2717–28
[67] Sadowski M and Albe K 2024 Grain boundary transport in the argyrodite-type Li_6PS_5Br Solid electrolyte: influence of misorientation and anion disorder on Li ion mobility *Adv. Mater. Interfaces* **11** 2400423
[68] Stejskal E O and Tanner J E 1965 Spin diffusion measurements: spin echoes in the presence of a time-dependent field gradient *J. Chem. Phys.* **42** 288–92
[69] Calaminus R, Harm S, Fabini D H, Balzat L G, Hatz A-K, Duppel V, Moudrakovski I and Lotsch B V 2022 Enhancing ionic conductivity by *in situ* formation of Li_7SiPS_8/argyrodite hybrid solid electrolytes *Chem. Mater.* **34** 7666–77
[70] Ramos E P, Bazak J D, Assoud A, Huq A, Goward G and Nazar L F 2022 Structure of the solid-state electrolyte $Li_{3+2x}P_{1-x}Al_xS_4$: lithium-ion transport properties in crystalline vs glassy phases *ACS Appl. Mater. Interfaces* **14** 56767–79
[71] Hood Z D, Kates C, Kirkham M, Adhikari S, Liang C and Holzwarth N A W 2016 Structural and electrolyte properties of $Li_4P_2S_6$ *Solid State Ion.* **284** 61–70
[72] Zhao F *et al* 2020 A versatile Sn-substituted argyrodite sulfide electrolyte for all-solid-state Li metal batteries *Adv. Energy Mater.* **10** 1903422
[73] Lewis J A, Tippens J, Cortes F J Q and McDowell M T 2019 Chemo-mechanical challenges in solid-state batteries *Trends Chem.* **1** 845–57
[74] Koerver R, Zhang W, de Biasi L, Schweidler S, Kondrakov A O, Kolling S, Brezesinski T, Hartmann P, Zeier W G and Janek J 2018 Chemo-mechanical expansion of lithium electrode materials-on the route to mechanically optimized all-solid-state batteries *Energy Environ. Sci.* **11** 2142–58